2020

Microscopic characteristics of magnetorheological fluids subjected to magnetic fields

Ningning Wang

Xinhua Liu

Shuaishuai Sun

Grzegorz Krolczyk

Zhixiong Li
University of Wollongong, lizhixio@uow.edu.au

See next page for additional authors

Microscopic characteristics of magnetorheological fluids subjected to magnetic fields

Abstract

© 2020 Elsevier B.V. With the aim of studying the microscopic characteristics of a magnetorheological fluid (MRF) in a magnetic field, the theoretical analyses of the particles dynamics in a magnetic field are presented, and a model for the particle motion is proposed. Based on these analyses, a three-dimensional numerical simulation of the microstructure of MRFs in different magnetic fields is performed. Furthermore, the microstructures of the MRFs are investigated using industrial computed tomography (CT) imaging. The numerical simulation and industrial CT results indicate that the chain structure of the same MRF becomes more apparent as the magnetic field strength increases, and in the same external magnetic field, this chain structure also becomes more apparent with an increase in the particle volume fraction. The lengths of particle chains in different magnetic fields are also captured in the industrial CT experiments. When the magnetic field strength is 12 mT, the particle chains of the MRF with a particle volume fraction of 30% reach more than 10 mm in length, which bridge the inner diameter of the container, and the dense clusters-like structure is formed, the clusters-like structure becomes denser with an increase in magnetic field. Moreover, the particle chain lengths of MRF with high particle volume fractions increase sharply with the magnetic field. The experiments demonstrated that the industrial CT is an efficient method to study the microstructures of MRFs by providing particle distributions of MRFs more clearly and intuitively.

Disciplines

Engineering | Science and Technology Studies

Publication Details

Wang, N., Liu, X., Sun, S., Krolczyk, G., Li, Z. & Li, W. (2020). Microscopic characteristics of magnetorheological fluids subjected to magnetic fields. Journal of Magnetism and Magnetic Materials, 501

Authors

Ningning Wang, Xinhua Liu, Shuaishuai Sun, Grzegorz Krolczyk, Zhixiong Li, and Weihua Li

Microscopic Characteristics of Magnetorheological Fluids Subjected to Magnetic Fields

Ningning Wang[1], Xinhua Liu[1*], Shuaishuai Sun[2], Grzegorz Królczyk[3], Zhixiong Li[4*], Weihua Li[4]

1. School of Mechanical and Electrical Engineering, China University of Mining & Technology, Xuzhou 221116, China

2. New Industry Creation Hatchery Center, Tohoku University, Sendai 980-8577, Japan

3. Department of Manufacturing Engineering and Automation Products, Opole University of Technology, Opole 45758, Poland

4. School of Mechanical, Materials, Mechatronic and Biomedical Engineering, University of Wollongong, Wollongong, New South Wales 2522, Australia

Corresponding Authors: zhixiong_li@uow.edu.au & liuxinhua@cumt.edu.cn

Abstract: With the aim of studying the microscopic characteristics of a magnetorheological fluid (MRF) in a magnetic field, the theoretical analyses of the particles dynamics in a magnetic field are presented, and a model for the particle motion is proposed. Based on these analyses, a three-dimensional numerical simulation of the microstructure of MRFs in different magnetic fields is performed. Furthermore, the microstructures of the MRFs are investigated using industrial computed tomography (CT) imaging. The numerical simulation and industrial CT results indicate that the chain structure of the same MRF becomes more apparent as the magnetic field strength increases, and in the same external magnetic field, this chain structure also becomes more apparent with an increase in the particle volume fraction. The lengths of particle chains in different magnetic fields are also captured in the industrial CT experiments. When the magnetic field strength is 12 mT, the particle chains of the MRF with a particle volume fraction of 30% reach more than 10 mm in length, which bridge the inner diameter of the container, and the dense clusters-like structure is formed, the clusters-like structure becomes denser with an increase in magnetic field. Moreover, the particle chain lengths of MRF with high particle volume fractions increase sharply with the magnetic field. The experiments demonstrated that the industrial CT is an efficient method to study the microstructures of MRFs by providing particle distributions of MRFs more clearly and intuitively.

Keywords: Microscopic characteristics; Magnetorheological fluid; Numerical simulation; Particle dynamics; Magnetic field; Industrial computed tomography

1. Introduction

Magnetorheological fluids (MRFs), as a type of solid–liquid two-phase smart material, are mainly formed by dispersing micron-grade magnetic particles into a carrier fluid, meanwhile, the stabilizers, antioxidants, thixotropic agents and lubricants are used as surfactant additives to improve its stability [1]. MRFs possess rheological behaviors. That is, without an applied magnetic field, the MRF is characterized as a Newtonian fluid, however, under an applied magnetic field, it instantly transforms from a free-flowing liquid into a semi-solid or solid, which presents a controllable yield strength [2, 3]. Moreover, these transformations are reversible [4]. MRFs are widely used in brake apparatus [5], controlled vibration dampers [6], sealing elements [7], polishing devices [8] and other engineering fields [9, 10] because of these properties.

It is widely recognized that the macroscopic properties of MRFs depend on their interior particle-formed microstructures [11, 12]. With the development of high–performance MRFs and the requirements of the working environment, the microstructures of MRFs require further understanding. In the past several decades, the understanding on the microstructures of MRFs has constantly advanced, and the research on their microscopic characteristics continues, however, the limitation of experimental methods and conditions severely restrict the research of their microscopic properties. As such, the previous electron microscopic, scanning electron microscopy (SEM), light microscopic examinations and x-ray diffraction are mostly focused in analyzing the inner structure and determining the phase constitution of this class of materials, these techniques have the inherent disadvantage of sample destruction, which do not allow the subsequent evaluation of the mechanical properties of MRFs. Additionally, the three-dimensional structural analysis is not allowed. An appropriate method to address these problems becomes an important research topic in recent years.

In the previous research on the microstructure of MR materials, the surface morphology of magnetorheological elastomers (MREs) composites was examined by computed tomography (CT) [13]. In [14], the effect of acetone contents on the MREs microstructure at the interfacial regions was investigated by using the three-dimensional nano-CT imaging. Similar to MRFs, MREs are a type of

multiphase multifunctional composite intelligent materials, which consist of an elastic matrix filled with micron-sized magnetic particles, and possess the similar high technical characteristics to MRFs, such as controllability, reversibility and rapid response, the sedimentation stability of MREs is better than MRFs [15, 16]. The primary goal of this study is the structural characterization of MRFs subjected to magnetic fields. In this paper, MRFs with different number of particles in three magnetic fields are numerically simulated firstly, then industrial CT imaging is used to observe the MRF particle distributions, which not only preserves the primary structures of the MRFs sample but also generates a three-dimensional map of the sample geometry. The particle dispersions of MRFs subjected to magnetic fields are reproduced intuitively and accurately.

2. Literature review

2.1. Research on microscopic characteristics of MR materials

Many studies and analyses of MRFs have been conducted toward understanding their microscopic characteristics and the effect of the microstructures on their macroscopic properties. Vagberg et al. [17] obtained the microstructure of MRFs at varying Mason number by taking snapshots. Tian et al. [18] researched the microstructures of magnetorheological elastomers with 0% and 15% weight fractions of silicone oil under a magnetic field that was rotated with a 45° angle by SEM, and found that the sample with 15% silicone oil contribution resulted in a less volume fraction of iron particles. Hu et al. [19] observed the microstructures of magnetorheological elastomers with curing agent weight ratio were 1:10, 1:20, 1:25 and 1:30 by SEM, and the results indicated that the carbonyl iron particles formed chain-like structures in matrix and they were assembled along the magnetic field direction. Pei et al. [20] researched the microstructure evolution of a superparamagnetic magnetic fluid based on Fe_3O_4-immobilized-SiO_2-nanospheres by the method of molecular dynamic. Zhao et al. [21] simulated the microstructures of magnetic fluids under the applied external magnetic field by the Monte Carlo method. Gharibvand et al. [22] tested the microstructures of MRFs in shear flow using dissipative particle dynamics, and found that the structures of particles were weakened as shear rates increased. Lagger et al. [23] gained insight into the microstructural behavior of a MRF under shear action using a discrete element simulation method, and found that the particles arranged in chains, sheet-like structures, or columns along the magnetic field lines. Hajalilou et al. [24] used x-ray diffraction and transmission electron microscopy to

evaluate the phase formation, structural and morphological changes for MRFs with Ni-Zn ferrite and Fe_3O_4 nanoparticle additive. Xu et al. [25] established a biphasic coarse-grained molecular dynamics model for MRFs, which including magnetic dipoles and abrasive particles. Meanwhile, the effects of magnetic field gradient, magnetic strength and abrasive particle concentration are studied both from theoretical analysis and numerical simulation. Liu et al. [26] simulated the three-dimensional microstructures of magnetic particles in different magnetic fields using Monte Carlo simulations and GPU accelerated technology. Li et al. [27] established the microscopic finite element model of MREs in two-dimension, and obtained the micrograph of the MREs by SEM. Xu et al. [28] established the theoretical model of particle motion of MREs in a magnetic field, and the movement simulation of two particles under a magnetic field is carried out. Chen et al [29] conducted micro-macro analysis of slip differential heat of MRFs including force, movement and heat between neighboring particles based on magnetic dipole and Hertzian contact theories.

2.2. Discussion

As detailed in the review of previous research, it is clear that current studies on the microscopic characteristics of MRFs and the similar materials are mainly focused on the experiments, analysis models and numerical simulations, which have achieved great progress. However, it is not allowed to do the subsequent evaluation of the mechanical properties by using the traditional experimental methods (SEM, light microscopic examinations and x-ray diffraction) due to the sample destruction. In this paper, a three–dimensional numerical simulation is used to calculate the microstructures of MRFs in magnetic fields, and the industrial CT is utilized to further analyze their microstructures.

Industrial CT is a nuclear imaging technology that can elucidate the internal structures, components, materials and defects of detected objects clearly and intuitively via two-dimensional cross-sectional or three-dimensional images in the absence of damage. At present, industrial CT is mainly used for nondestructive inspection of samples, materials processing and mineral research. Tang et al. [30] observed the pore structure of permeable brick by using industrial CT. Cui et al. [31] researched the fractures and minerals in subbituminous and bituminous coals by industrial CT. Kou et al. [32] used industrial CT to determine the microscopic relaxation dynamics of hard granular ellipsoids subjected to an oscillatory shear.

3. Dynamical model and numerical simulation

3.1. Dynamical model

When a magnetic particle with a radius R is placed into a uniform external magnetic field H, the magnetic moment $\boldsymbol{m}$ of this particle can be expressed as follows [11, 28]:

$$\boldsymbol{m} = V\boldsymbol{M} = \frac{4}{3}\pi R^3 \chi H, \tag{1}$$

where $V = \frac{4}{3}\pi R^3$, $\boldsymbol{M} = \chi H$ and χ are the volume of the particle, magnetization of the particle and magnetic susceptibility.

Considering the influence of additional magnetic fields produced by other particles, the magnetic force F_1 can be obtained by the enhanced dipole model, which is expressed as follows [33]:

$$\boldsymbol{F_1} = \sum_{\substack{i=1 \\ j\neq 1}}^{N} \frac{4\pi\mu_0 R^6 H^2 \chi^2}{3r_{ij}^5} \left\{ \left[(1 - 5\cos^2\theta) - \frac{R^3\chi}{3r_{ij}^3}(1 + 4\cos^2\theta) \right] \boldsymbol{r}_{ij} + 2r_{ij}\cos\theta \left(1 + \frac{R^3\chi}{6r_{ij}^3} \right) \boldsymbol{k} \right\}, \tag{2}$$

where μ_0, r_{ij}, $\boldsymbol{r}_{ij}$, θ and $\boldsymbol{k}$ are the magnetic permeability in a vacuum, the relative position from particle i to particle j, the relative position vector from particle i to particle j, the angle between the center connecting line of two particles and the external magnetic field and the unit vector of the external magnetic field, respectively.

During the motion process, a repulsive force is produced due to the collision of the particles. Ignoring the friction between the particles, the repulsive force F_2 can be expressed as follows [34]:

$$\boldsymbol{F_2} = \sum_{j\neq i} \frac{3\mu_0 m^2}{32\pi R^4} exp\left[-\beta \left(\frac{r_{ij}}{2R} - 1 \right) \right] \hat{\boldsymbol{r}}_{\boldsymbol{ij}}, \tag{3}$$

where β is a material parameter, which represents how fast or slow the repulsive force increases, $m = \|\boldsymbol{m}\|$ and $\hat{\boldsymbol{r}}_{\boldsymbol{ij}} = \frac{\boldsymbol{r_{ij}}}{r_{ij}}$ are the Euclidean norm of magnetic moment $\boldsymbol{m}$ and the unit vector of the relative position of the two particles, respectively.

MRFs are usually incompressible viscous liquids. Thus, when the particles move in the matrix, the viscous resistance of the particles can be described by the Stokes equation [11, 29]:

$$\boldsymbol{F_3} = -6\pi R\eta\boldsymbol{v}, \tag{4}$$

where η is the viscosity coefficient of the matrix and $\boldsymbol{v}$ is the velocity vector of the magnetic particles.

The gravity and buoyancy forces of magnetic particles can be expressed by Equations (5) and (6) , respectively:

$$\boldsymbol{F_4} = \frac{4}{3}\pi R^3 \rho_1 g, \tag{5}$$

$$\boldsymbol{F_5} = \frac{4}{3}\pi R^3 \rho_2 g \mathbf{z}, \tag{6}$$

where ρ_1 and ρ_2 are the density of magnetic particles and matrix, respectively. g is the gravitational acceleration, $\boldsymbol{z}$ is the unit vector in the vertically upward direction.

In order to reduce the calculation process, the effect of gravity and buoyancy forces on particle motion are defined, which is performed by comparing the ratios of the maximum magnetic forces of a magnetic particle with the gravity and buoyancy forces under different magnetic fields, respectively. The parameters used in the simulation are listed in Table 1. The ratio λ of the maximum magnetic forces of a magnetic particle with the gravity and buoyancy forces are shown in Figure 1. Figure 1 indicated that the magnetic forces were much stronger than gravity and buoyancy forces, and the ratio increased with the magnetic field strength, which demonstrated that effect of gravity and buoyancy forces could be ignored in the simulation. The Brownian force also has very small contribution to the resultant force on particles, which is not considered in the simulation [28, 35].

Table 1. Simulation parameters.

Parameter	**Parameter value**	**Parameter**	**Parameter value**
μ_0 (H · m^{-1})	$4\pi \times 10^{-7}$	R (μm)	8
η (Pa · s)	0.001	$\rho_1 (kg \cdot m^{-3})$	7.86×10^3
χ	1.0	β	10
T (K)	298	$\rho_2 (kg \cdot m^{-3})$	0.97×10^3

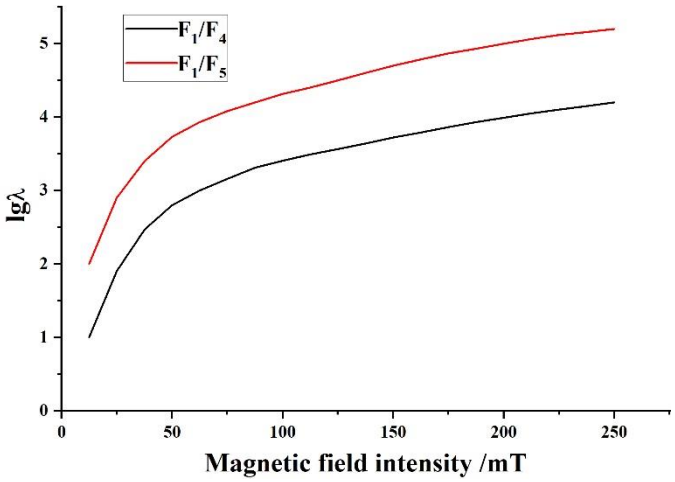

Figure 1. The ratio of the maximum magnetic force of a magnetic particle with the gravity and buoyancy forces under different magnetic fields.

Based on Equations (1) – (4) and Newton's Second Law, the dynamical equation of the particles can be expressed as follows:

$$m_1\boldsymbol{a} = m_1\frac{d^2u}{dt^2} = \boldsymbol{F_1} + \boldsymbol{F_2} + \boldsymbol{F_3}, \tag{7}$$

where $m_1 = \rho_1 V$ is the mass of a particle, $\boldsymbol{a}$ is the acceleration of a particle.

3.2. Simulation algorithm

Without an external magnetic field, the magnetic particles are distributed randomly in the matrix. The particles are in a steady state, as their initial velocities are $v = 0$ without considering the Brownian motion. Once an external magnetic field is applied, the magnetic particles are magnetized into magnetic dipoles, and the particles are accelerated under the combined action of magnetic force, viscous resistance and repulsive force. Then, the corresponding velocity and displacement are derived, which changes the combined action forces as a result. In turn, the derived velocity and displacement are also changed. These steps iterate until the system reaches a stable equilibrium. In this paper, the velocity Verlet algorithm [36, 37] is used to calculate the dynamical equation, which obtains the position and velocity of each particle simultaneously without losing accuracy. The velocity Verlet algorithm in this paper is stated as follows:

The initial position $\boldsymbol{u}$ of a particle is

$$\{\boldsymbol{u} = \hat{\boldsymbol{u}} | t = 0\}, \tag{8}$$

where $\hat{\boldsymbol{u}}$ is generated by a random function.

The initial velocity $\boldsymbol{v}$ of a particle is

$$\{\boldsymbol{v} = 0 | t = 0\}. \tag{9}$$

173 The acceleration $\boldsymbol{a}$ of a particle at time t is

$$\boldsymbol{a}(t) = \frac{\boldsymbol{F_1}(t) + \boldsymbol{F_2}(t) + \boldsymbol{F_3}(t)}{m_1}. \tag{10}$$

174 Assuming the increment of time used in this simulation is $\Delta \boldsymbol{t}$, the position $\boldsymbol{u}$ and the velocity

175 $\boldsymbol{v}$ of the particle in time $\boldsymbol{t} + \Delta \boldsymbol{t}$ can be expressed as follows:

$$\boldsymbol{u}(t + \Delta t) = \boldsymbol{u}(t) + \boldsymbol{v}(t)\Delta t + \frac{\mathbf{1}}{\mathbf{2}}\boldsymbol{a}(t)\Delta t^2, \tag{11}$$

$$\boldsymbol{v}(t + \Delta t) = \boldsymbol{v}(t) + \frac{\mathbf{1}}{\mathbf{2}}[\boldsymbol{a}(t) + \boldsymbol{a}(t + \Delta t)]\Delta t. \tag{12}$$

176 The position, velocity and resultant force of the particles are constantly updated, and Equations
177 (8) – (12) are iterated until the system reaches a steady state.

178 In order to define the number of time step and the stable equilibrium state of the simulation, the
179 energy equations of the particles are introduced. Under the action of an external magnetic field *H*,
180 particles are magnetized and moved. During this process, the energy of the particles changes. The
181 involved energies include magnetic field energy**,** interaction energy of the neighboring particles and
182 the repulsive energy [26].

183 the magnetic energy is generated by the action of an external magnetic field *H*, which is shown
184 as follows [21]:

$$U_1 = -\mu_0 \boldsymbol{m_i} H, \tag{13}$$

185 where $\boldsymbol{m_i}$ is the magnetic moment of particle *i*.

186 The repulsive energy is generated by the collision between particles, which is expressed as
187 follows [21, 26]:

$$U_2 = \pi d^2 \xi k_B T \left\{1 - \frac{r_{ij} - d}{2\delta} - \frac{r_{ij}}{2\delta} In\left(\frac{d + 2\delta}{r_{ij}}\right)\right\}, \tag{14}$$

188 where k_B is the Boltzmann constant, and $k_B = 1.38 \times 10^{-23}$ J/K, *d* is the diameter of a particle,
189 ξ is the number of surfactant molecules per unit area, δ is the thickness of the magnetic particle
190 surfactant layer, and $\delta = 0.05$ μm.

191 The interaction energy of the neighboring particles is shown as follows [21, 26]:

$$U_3 = \frac{\mu_0 m^2}{4\pi r_{ij}^3}\{\boldsymbol{n_i}\cdot\boldsymbol{n_j} - 3(\boldsymbol{n_i}\cdot\boldsymbol{r_{ij}})\cdot(\boldsymbol{n_j}\cdot\boldsymbol{r_{ij}})\}, \quad (15)$$

where the $\boldsymbol{n_i}$ and $\boldsymbol{n_j}$ are the unit vector given by $\boldsymbol{n_i} = \boldsymbol{m_i}/m$ and $\boldsymbol{n_j} = \boldsymbol{m_j}/m$, respectively.

The energy of the total system can be calculated as:

$$U = \sum_{i=1}^{n} U_i. \quad (16)$$

In the simulation, each particle is described by a motion quantity in every step. Energy before and after the particle moves are set as U_4 and U_5, respectively. If $U_5 < U_4$, this motion quantity will be effective. If not, the quantity may be effective with a probability of $\boldsymbol{exp}\left(-\frac{\boldsymbol{U_5-U_4}}{\boldsymbol{k_BT}}\right)$ [21, 26]. When total energy changes a little, structure is considered to be a stable equilibrium state, and this structure is the ultimate. The detailed calculation flow is presented in Figure 2.

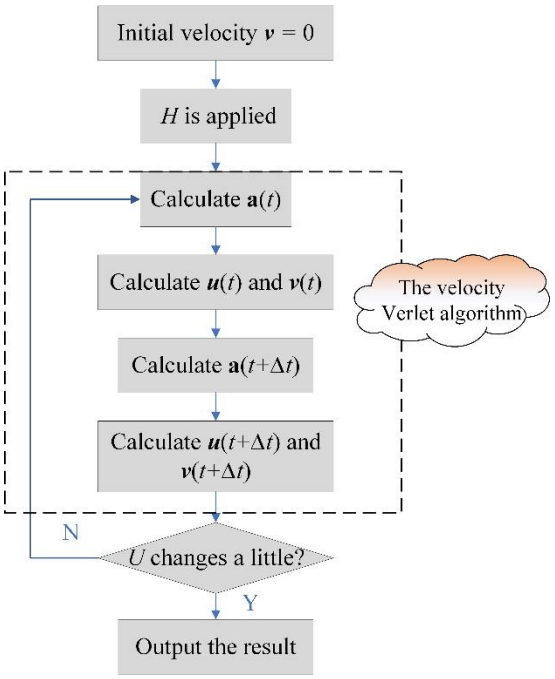

Figure 2. Calculation flow of the numerical simulation

3.3. The method for saving computational time and choosing the time increment

A complete simulation is a time consuming process, because the computation of the forces on particle *i* is related to the interaction between the particle *i* and all other particles. In an MRF system with the number of particles is *N*, the interactions need to be computed in each increment is *N(N-1)/2* without any technical method.

Eq. (2) indicates that the magnetic force between two dipolar particle sharply decreases with the

increase of the distance between them, as shown in Figure 3, where r is the distance between two dipolar particles. The magnetic force between the two dipolar particles will tend to vanish if r is sufficiently large.

In order to save computing time, link-cell and Verlet list methods are used to improve computing efficiency, as shown in Figure 4, the computation region is separated into many small square cells of size r_i, which is defined as the cut off distance. It can be seen from Figure 3 that if the distance between two dipolar particles is more than $6R$, the magnetic force between the two dipolar particles is pretty small, which could be negligible. Therefore, $r_i = 6R$ is used in computation. In the simulation system, all the particles are located in a cell, and a particle which interacts with particle i should be in the shadow region, as the search for the interacting particles only covers 3 x 3 x 3 cells for a 3-D problem or 3 x 3 cells for a 2-D problem. Subsequently, a judgement need to be determined is whether other particles in these cells are out of the cut off circle or not, and a Verlet list for particle i is produced at the same time.

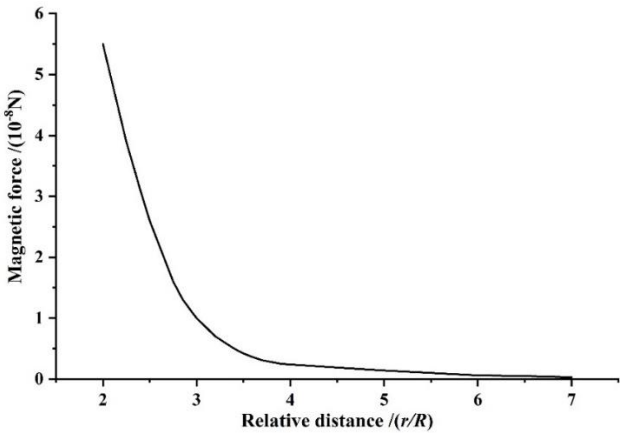

Figure 3. The relationship between magnetic force and r/R.

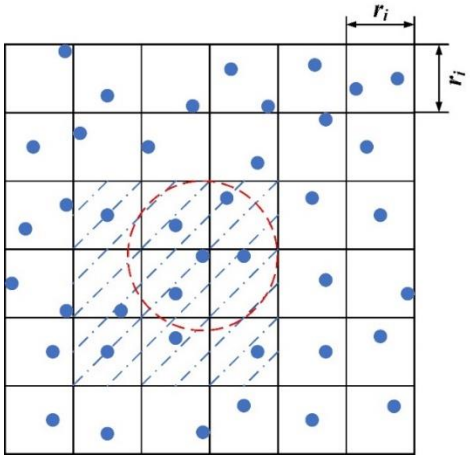

Figure 4. The schematic for the combined link cell and Verlet list method.

A proper time increment affects the results of simulation, in each time increment, the velocity and the position of each particle will update using the equation of motion and the forces on the particle. A relative small time increment can result in an unnecessary consumption of time, and a relative big time increment affects the convergence of computation and results in an incorrect result. The magnetic force between dipolar particles involves very strong non-linearity, which makes the choice of a proper time increment is of critical importance.

The distance between particles strongly affects the stability of computation. The fact that the magnetic force increases sharply with the decrease of the distance between two particles, and If a fixed time increment is applied in the simulation, either the simulation time increases greatly, or the two particles may overlap and even pass through each other. Moreover, it is difficult to choose a fixed time increment because the positions of particles change continuously and the relative distances between different particles are various. In this paper, the variable time increment is used in the simulation. The variable time increment is determined by the maximum gradient of the resultant force [38], which is performed by examining the curvature at the minimum of the potential well when two particles aligned in the direction of the applied magnetic field. Assuming two nearby particles start and approach each other due to the attractive force between the two particles and contact each other in $\Delta\bar{t}$, if the resultant forces on one particle at time t and $t+\Delta\bar{t}$ are $F(t)$ and $F(t+\Delta\bar{t})$, respectively, the time increment $\Delta\bar{t}$ is determined with $\Delta\bar{t} = 2\sqrt{m\left|\frac{dF(r)}{dr}\right|_{r=r_0}^{-1}}$, where r_0 is the distance between the two particles when they contact each other.

3.4. Simulation results and analysis

In this simulation, the simulated objects were cubes with side lengths that were set to 1 mm. A cube contained magnetic particles and a matrix, where the magnetic particles were all spherical**.** In the absence of a magnetic field, the magnetic particles were distributed randomly in the cube. In order to calculate the interaction between the walls of cube and particles, it was assumed that the walls were covered with particles, then the forces between the particles and the walls could be cleverly replaced by the interaction between the particles. In the simulation, a particle microcosmic system with a smaller order of magnitude was simulated to provide the media information similar to the macroscopic properties of MRF. In order to make the simulation results closer to the actual effect, the

periodic boundary condition was applied, which was as a particle system was regarded as a cube, and it was surrounded by other same cubes.

Three types of MRFs with particle numbers of 500, 1000 and 1500 were simulated with an applied magnetic field in this section. Figure 5 shows the energy variation of three MRFs systems in an external magnetic field. In Figure 5, it indicated that total energy of MRF reduced as the number of simulation steps increased. The structure of MRFs could be considered stable when number of simulation step was 50000. The simulation results of three types of MRFs after 50000 steps are shown in Figures 6–8.

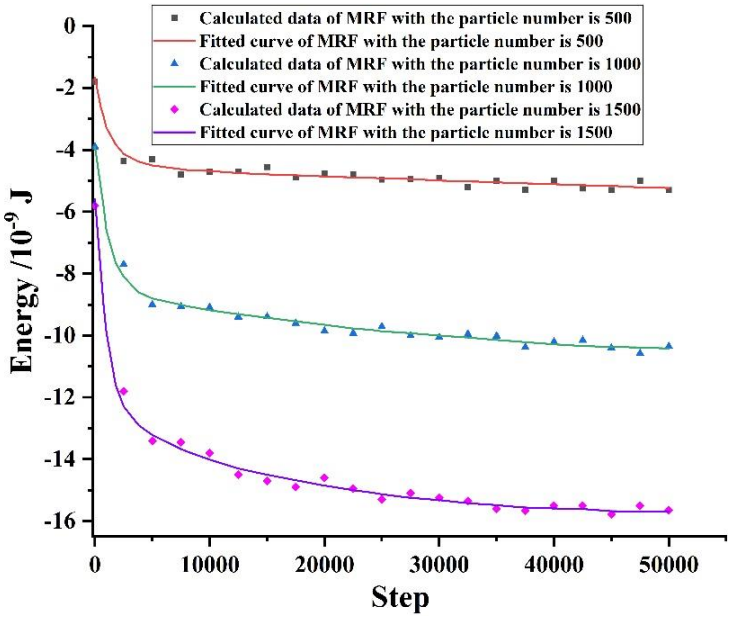

Figure 5. Energy variation curves of three types MRFs system in an external magnetic field.

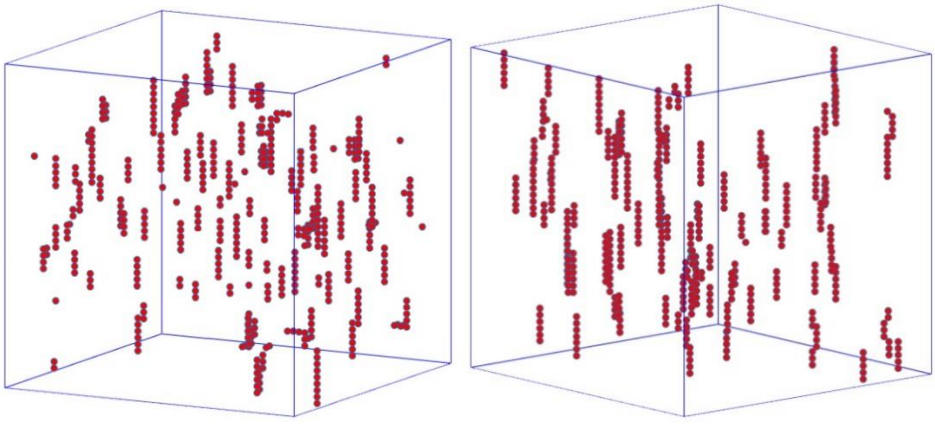

(a) (b)

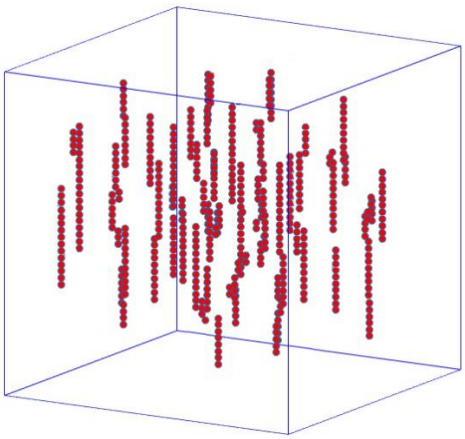

(c)

Figure 6. Simulation results of a cube containing 500 MRF particles in differing magnetic field. (a) B = 6 mT, (b) B = 12 mT, (c) B = 18 mT.

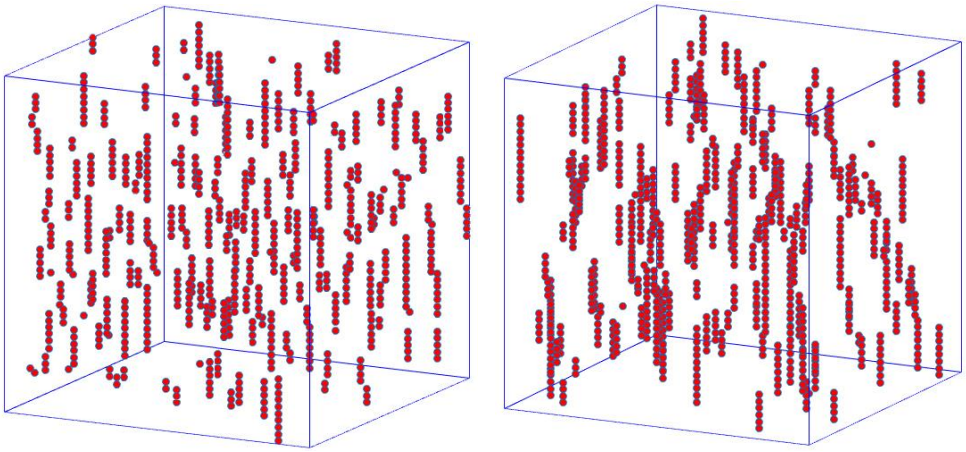

(a) (b)

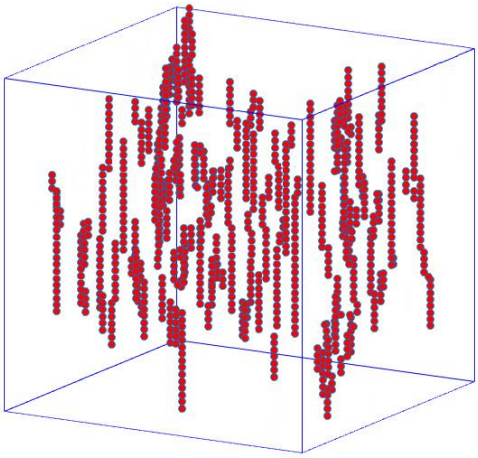

(c)

Figure 7. Simulation results of a cube containing 1000 MRF particles in differing magnetic field. (a) B = 6 mT, (b) B = 12 mT, (c) B = 18 mT.

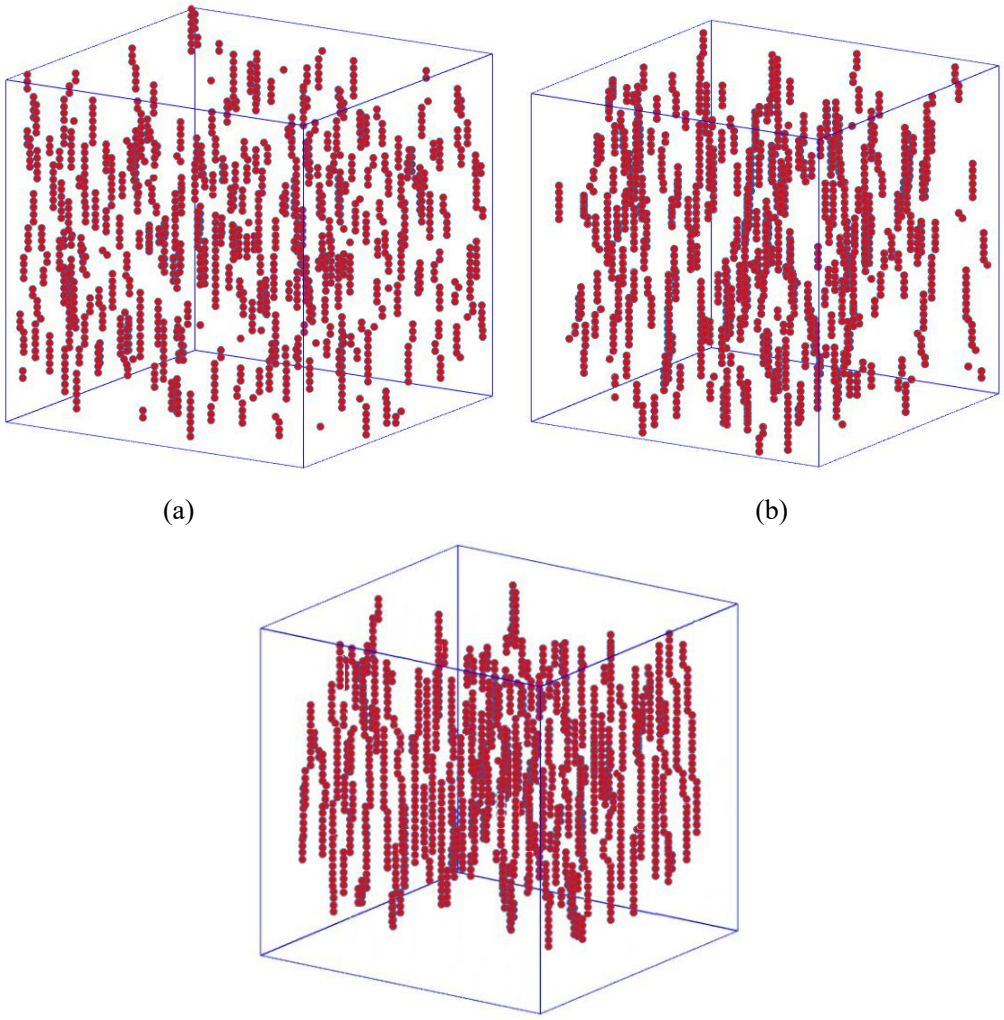

(a) (b)

(c)

Figure 8. Simulation results of a cube containing 1500 MRF particles in differing magnetic field. (a) B = 6 mT, (b) B = 12 mT, (c) B = 18 mT.

Figures 6–8 indicated that the MRFs with different volume fractions presented a similar variation phenomenon when the magnetic field strength increased from 6 mT to 18 mT. In a 6 mT magnetic field, the magnetic particles began to form chains. However, the chains were relatively short, with lengths of 4–8 particles accounting for the largest proportion, and individual particles still existed in the matrix. When the magnetic field strength increased to 12 mT, the number of short chains began to decrease, and the number of long chains began to increase. At this point, almost no single particles remained in the matrix. When the magnetic field strength increased to 18 mT, the chain lengths increased significantly, growing by 1.5 to 2 times in length compared with the chains in the 12 mT magnetic field. Furthermore, it was clear that some particle chains combined to form bundled and clustered structures. In the same magnetic field, the numbers and lengths of particle chains presented

an increasing trend with the increasing particle volume fraction, which was obvious when the magnetic field strength increased to 18 mT.

4. Experimental

4.1. Materials and instrumentation

The MRFs for this experiment were the silicone oil-based MRFs GH-MRF-250, GH-MRF-350 and GH-MRF-450, which were purchased from Zhang Dongnan Studio. In these MRFs, soft magnetic carbonyl iron particles (average diameter: 8 μm, density: 7.86 g/cm^3; Beijing DK Nano Technology Co., Ltd.) were used as a dispersed phase, dimethyl silicone oil (viscosity: 500 cSt at 25 °C, density: 0.97 g/cm^3; Shin-Etsu, Japan) was used as suspending medium, sodium dodecyl benzene sulfonate and oleic acid supplied were used as surfactant to improve the sedimentation stability and reduce aggregation, diatomite powders and graphite were used as inorganic thixotropic agent and antiwear agent. The corresponding volume fractions of magnetic particles in GH-MRF-250, GH-MRF-350 and GH-MRF-450 were 20%, 30% and 40%, respectively. Their zero field viscosity were 242.5 mPas, 382.5 mPas and 688.3 mPas, respectively. The working temperature was –40–150 °C. The magnetization curves of the three types of MRFs are shown in Figure 9.

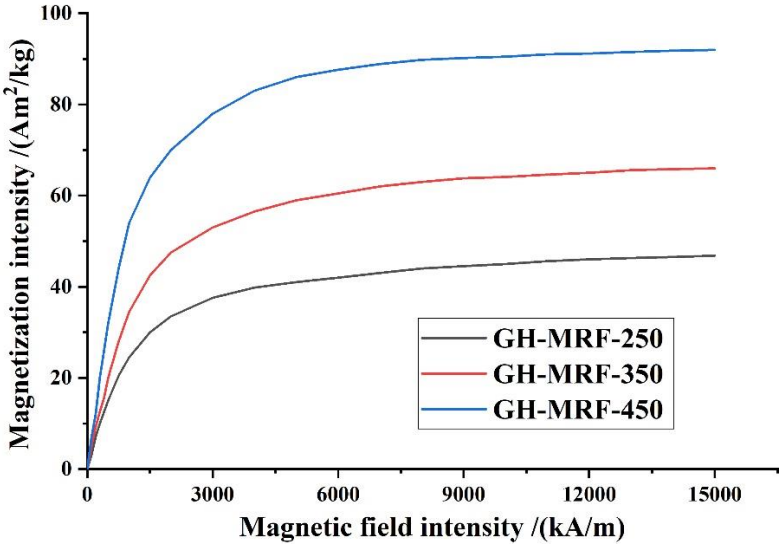

Figure 9. Magnetization curves of the three types of MRFs.

This experiment was performed through an x-ray microtomography system (X5000, North Star Imaging, Inc.). The system possessed a large scanning envelop and could load sizable objects while maintaining enough sensitivity to inspect very small items. In the experiments, the cone beam x-ray was applied to scan the samples with the step-by-step method at 360°. The x-ray tube was Micro-

focus, the voltage and current of the x-rays were 200 kV and 150 μA, respectively. The effective spatial resolution of the system was better than 0.5 μm after geometric magnification (greater than 2000×), and the minimum focal spot size was smaller than 0.5 μm. The distance between the MRFs and the x-ray source and between the MRFs and the detector were set to 116 mm and 430 mm, respectively, which were the most appropriate locations for imaging according to manufacturer's recommendation. The scanning period was set to 90 min. During this period, 1800 projection images were obtained to synthesize a three-dimensional image. The detailed experimental system is shown in Figure 10.

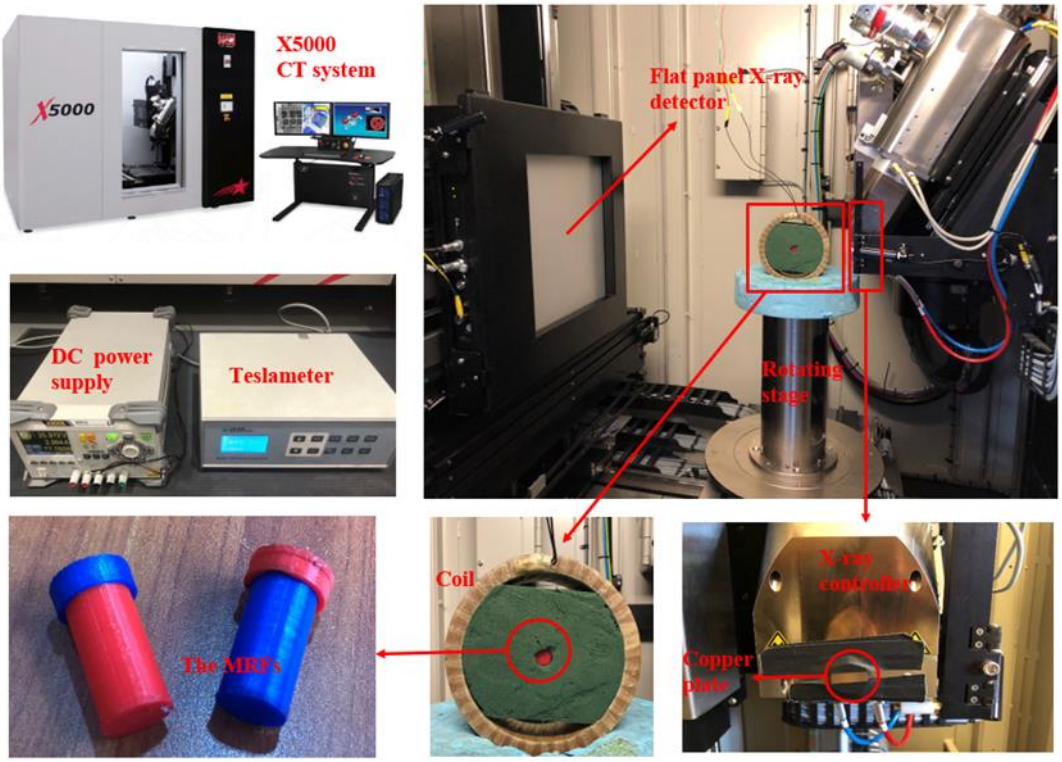

Figure 10. Industrial CT experimental system.

As shown in Figure 10, the MRF was filled into a cylindrical container (volume = 1.57 mm^3, cross-sectional diameter = 10 mm) which was made of acrylonitrile butadiene styrene plastic. The container was placed in the center of the coil and supported by green pearly foam. The inner diameter, outer diameter, height, number of turns and wire diameter were 140 mm, 180 mm, 70 mm, 1500 and 1 mm, respectively. The coil with the MRF was placed on a computer numerical control stage, which could rotate 360° repeatedly around its central axis. The cone beam x-ray was launched by the x-ray controller and passed through the coil and the MRF, at last, it received by the flat panel detector. A circular copper plate with a thickness of 3 mm and a diameter of 30 mm was pasted in the x-ray

emitter, which is used to compensate for the overexposure area where the x-ray was not blocked by the coil during the scanning process. The DC power supply and the teslameter were used to provide current to the coil and to measure the magnetic field of the scanned object, respectively. The CT scanning process is shown in Figure 11.

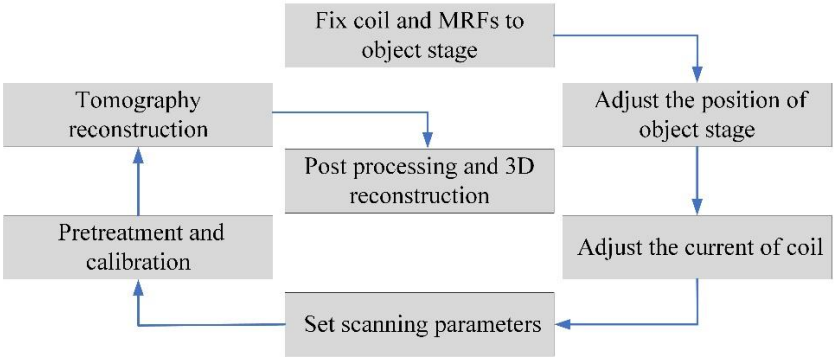

Figure 11. The scheme of CT scanning process.

4.2. Experimental results and analysis

Using the experimental parameters detailed in the previous section, three types of MRFs were scanned with external magnetic fields of 0 mT, 6 mT, 12 mT and 18 mT, respectively. The automatic data collection, volume processing, reconstruct the inverse projection of the three-dimensional structures and length capture of the particle chains were conducted in the NSI analysis software EFX-CT. The scanning result of the GH-MRF-350 in a 12 mT external magnetic field is shown in Figure 12, and the scanning results of the GH-MRF-250, GH-MRF-350 and GH-MRF-450 in the 0 mT magnetic field are shown in Figure 13.

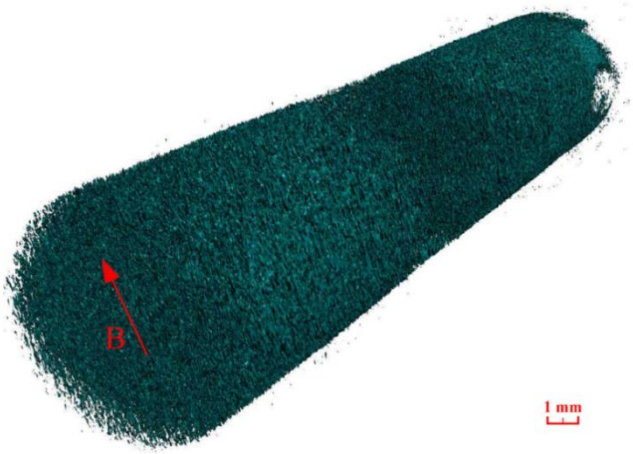

Figure 12. Scanning results of GH-MRF-350 in a 12 mT external magnetic field.

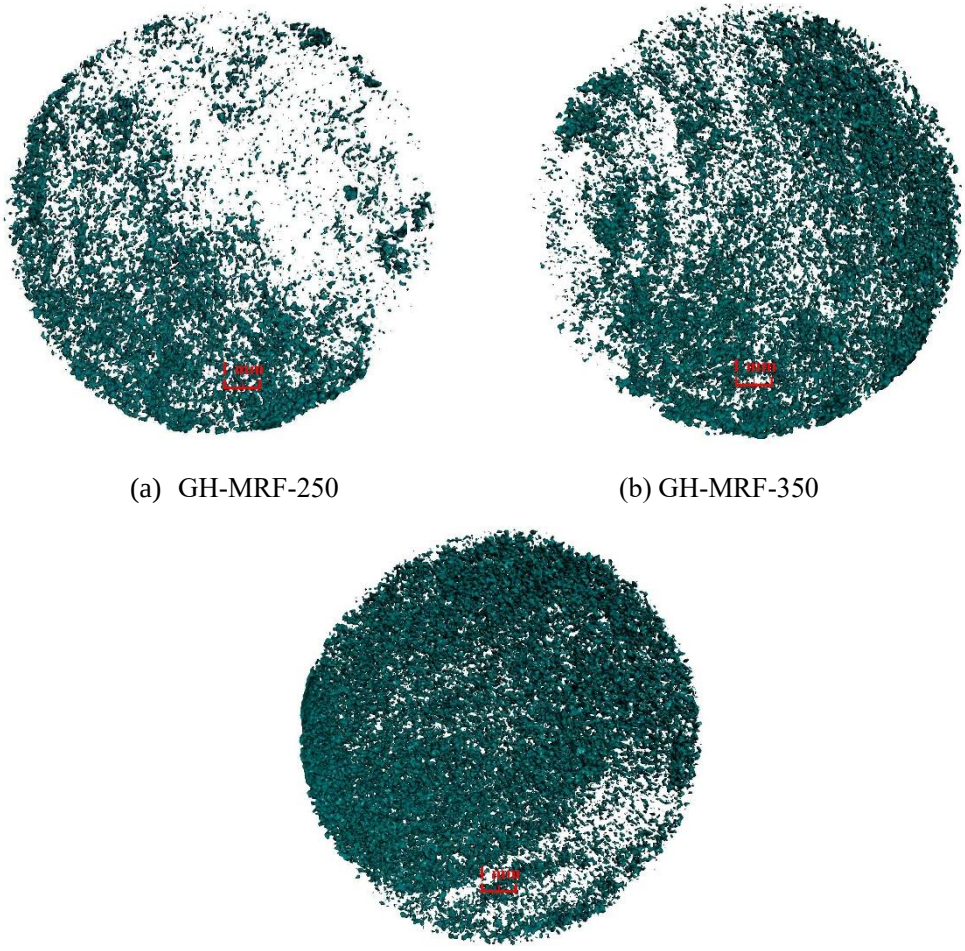

(a) GH-MRF-250 (b) GH-MRF-350

(c) GH-MRF-450

Figure 13. Particle distribution of three types of MRFs in a 0 mT external magnetic field.

Figure 13 indicated that the magnetic particles were distributed irregularly when no external magnetic field was applied, and the particle distribution was uneven in each MRF sample. Meanwhile, some particles condensed into a flocculent structure. The irregular shapes and size difference of the particles were due to image artifacts, wherein the distance between particles was too short to be recognized and the adjacent particles were identified as a whole.

In this experiment, the information of the particle distributions anywhere in the scanned object could be obtained, this process was similar to extracting relevant information from three-dimensional models in the corresponding modeling software, which was more convenient and intuitive than the previous experimental methods [17-19]. Furthermore, particle distributions could be quantitatively analyzed in this experiment. To better analyze and compare the particle distributions of the MRFs, a cylinder in the scanning result was extracted, and the relevant figures in different rotation angles were used to exhibit the scanning results, as shown in Figure 14. Figures 15–23 show the scanning results

for the three types of MRFs in 6 mT, 12 mT and 18 mT magnetic fields, which presented a corresponding relation with Figure 14. Figure 24 showed the variation curves of particle chain lengths with the magnetic fields.

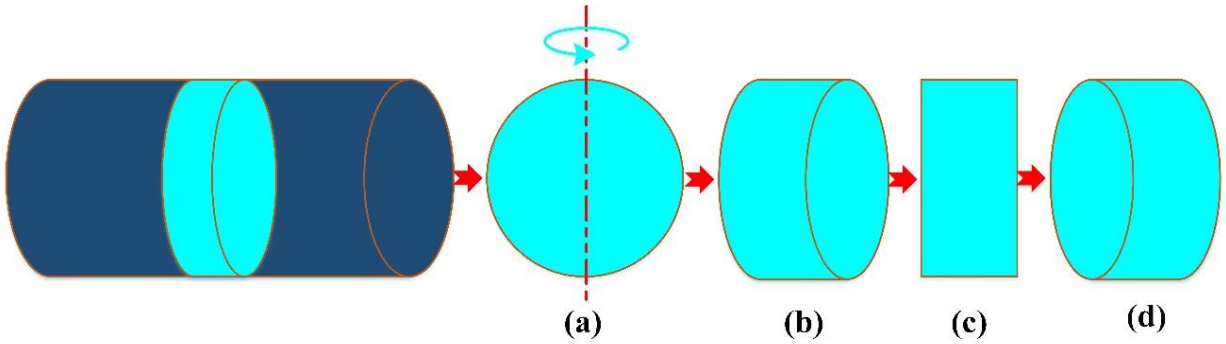

Figure 14. The extracted objects.

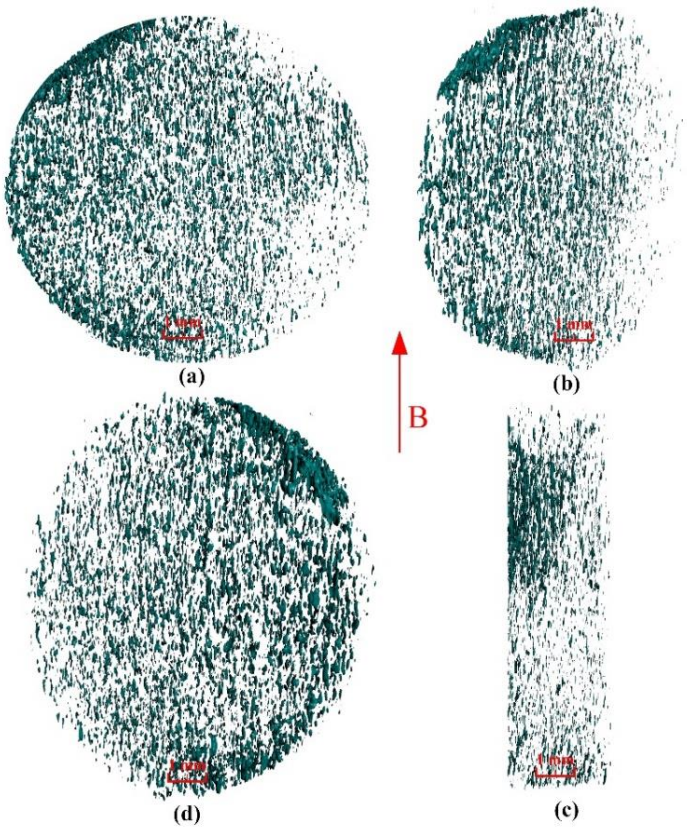

Figure 15. Experimental images of GH-MRF-250 in a magnetic field B = 6 mT.

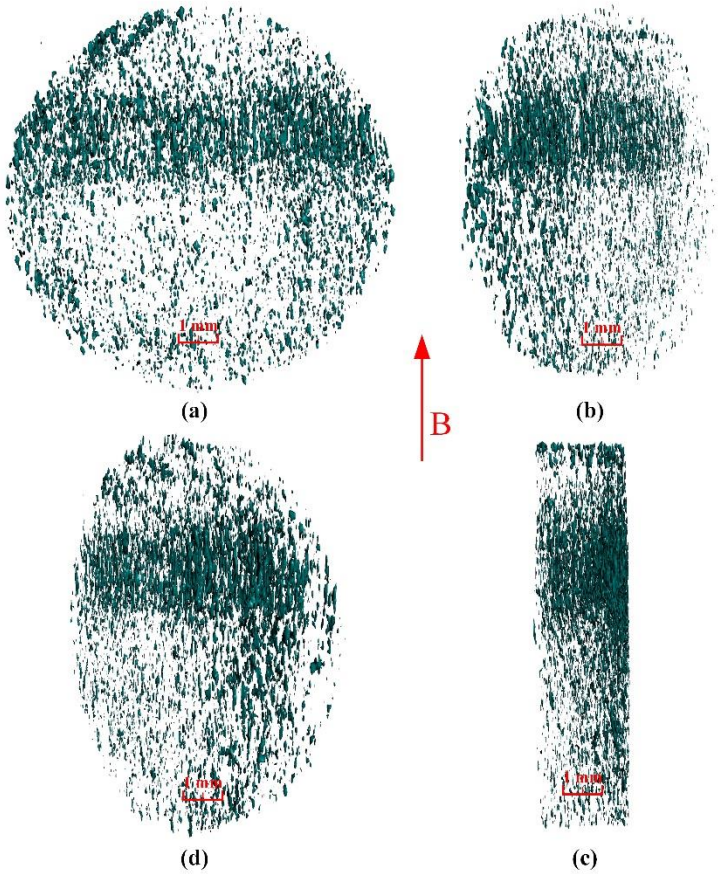

Figure 16. Experimental images of GH-MRF-250 in a magnetic field B = 12 mT.

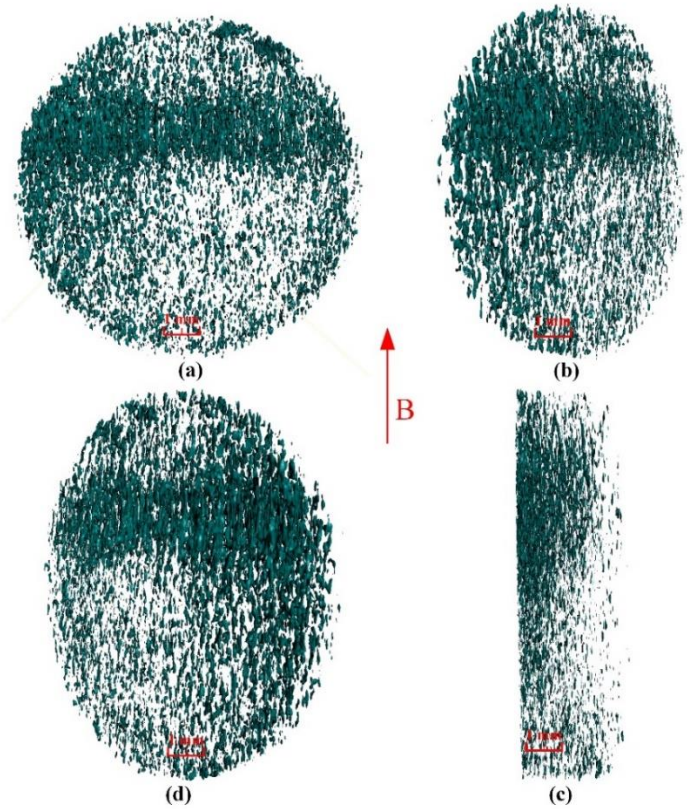

Figure 17. Experimental images of GH-MRF-250 in a magnetic field B = 18 mT.

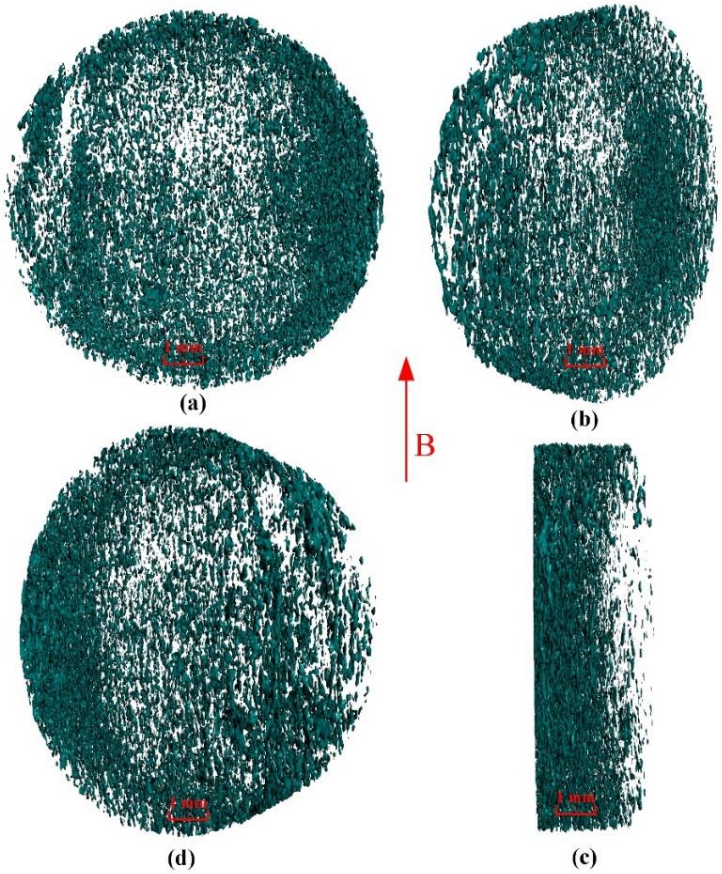

374

375 Figure 18. Experimental images of GH-MRF-350 in a magnetic field B = 6 mT.

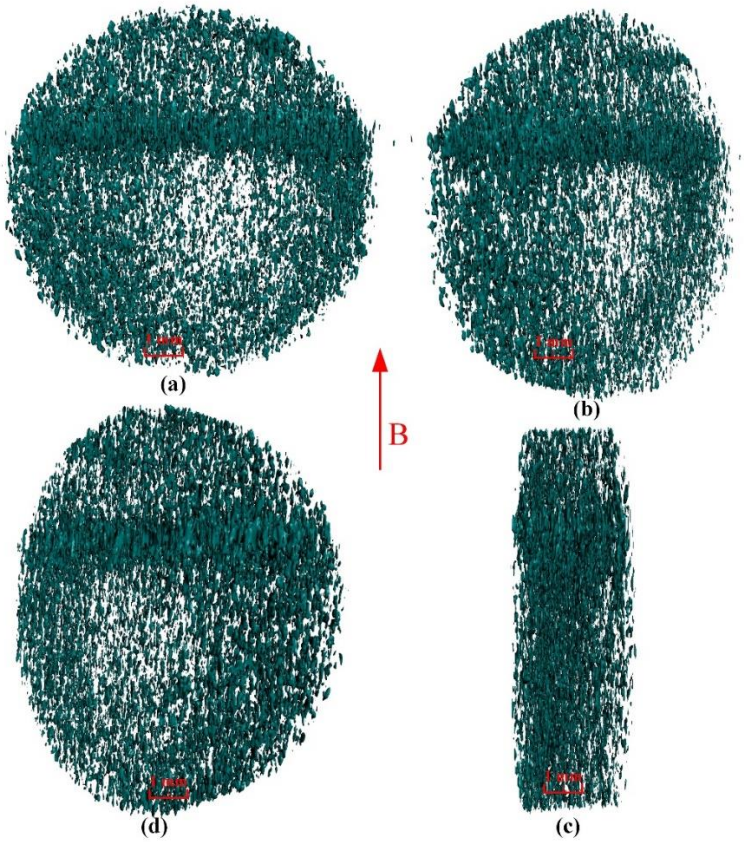

376

377 Figure 19. Experimental images of GH-MRF-350 in a magnetic field B = 12 mT.

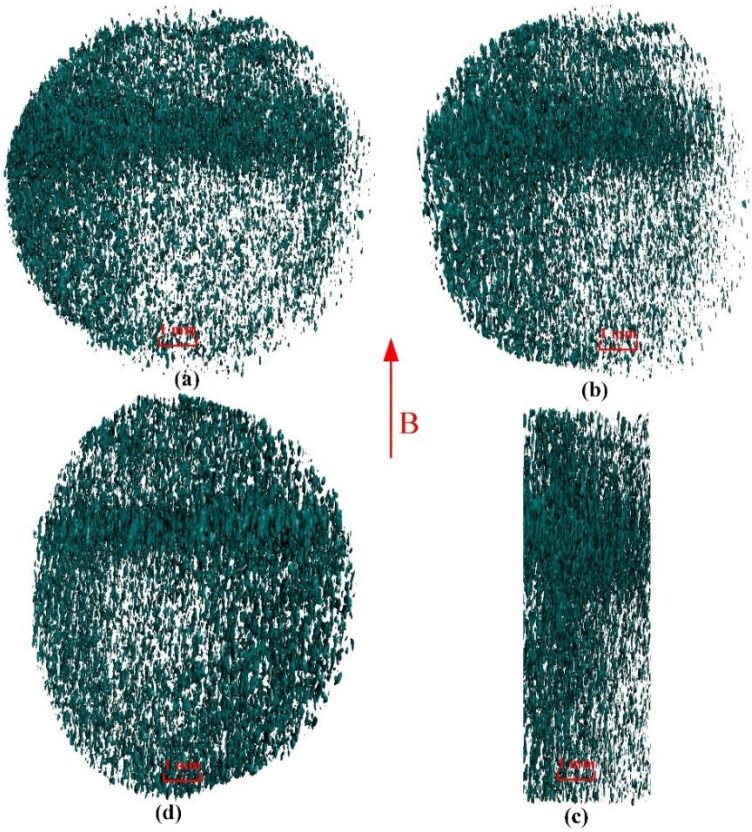

Figure 20. Experimental images of GH-MRF-350 in a magnetic field B = 18 mT.

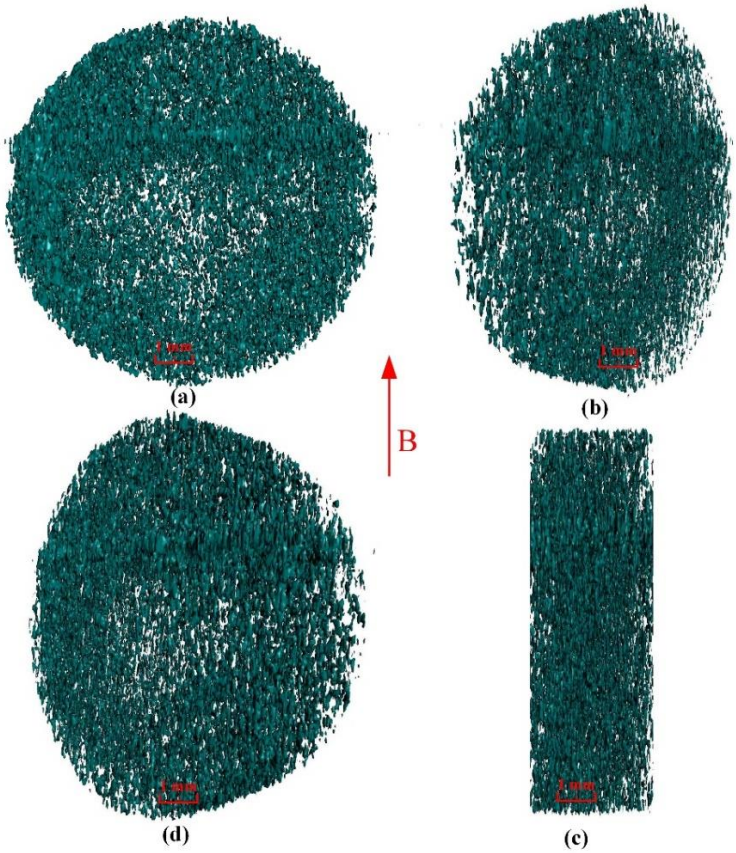

Figure 21. Experimental images of GH-MRF-450 in a magnetic field B = 6 mT.

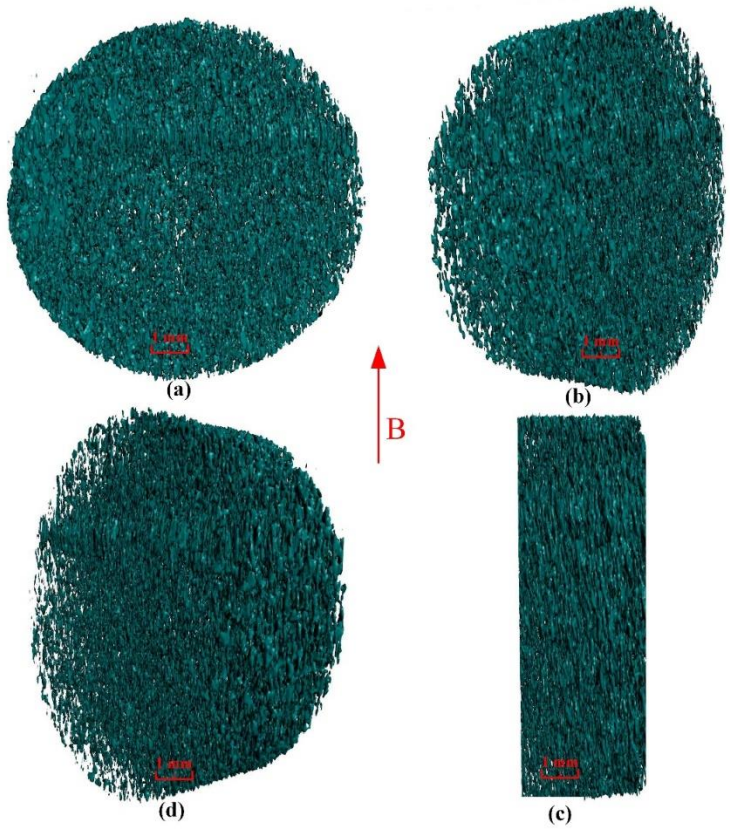

Figure 22. Experimental images of GH-MRF-450 in a magnetic field B = 12 mT.

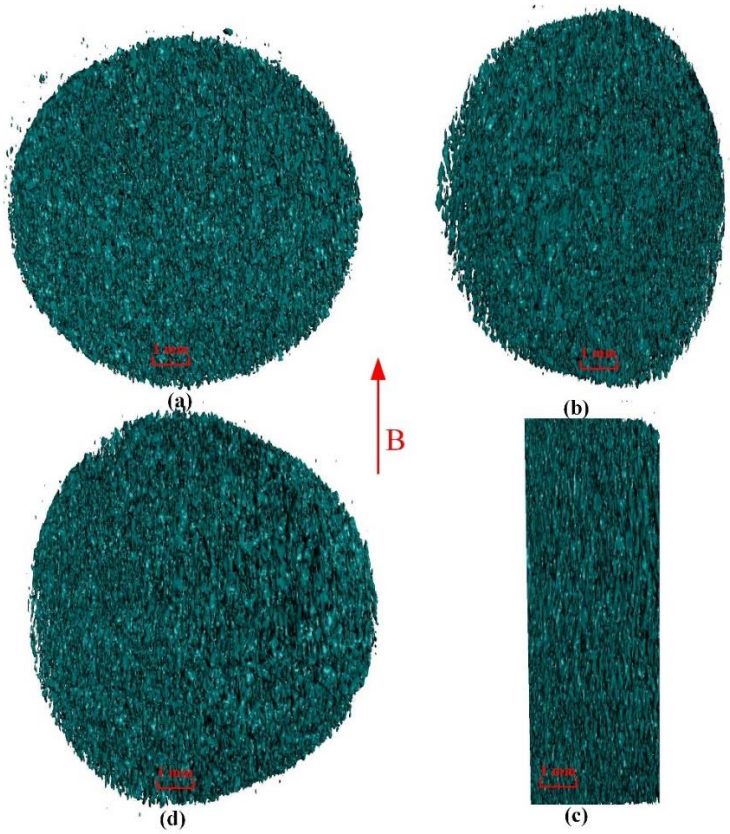

Figure 23. Experimental images of GH-MRF-450 in a magnetic field B = 18 mT.

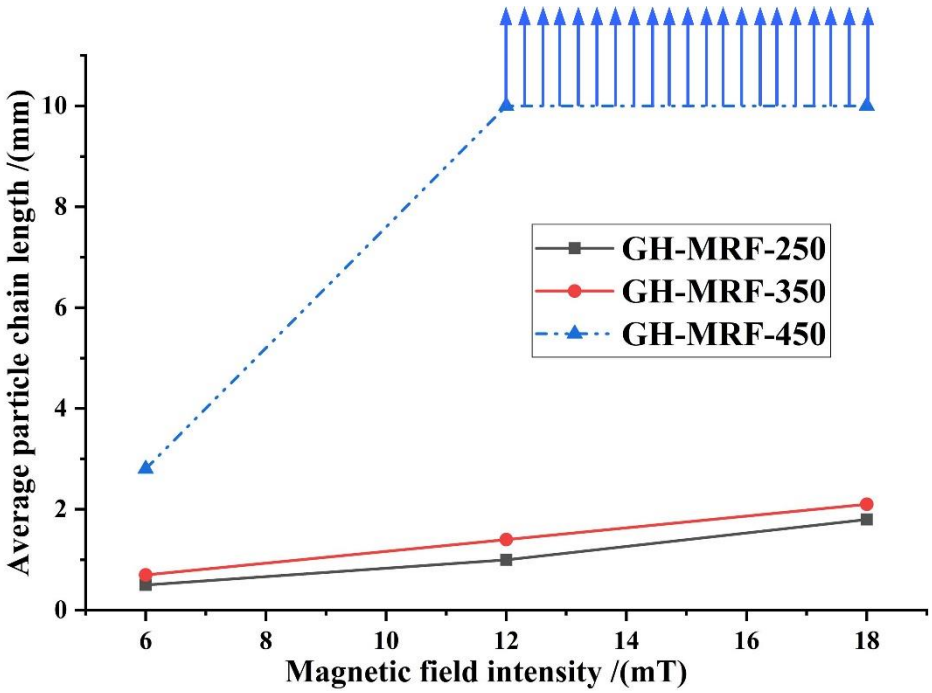

Figure 24. The variation of particle chain lengths with the magnetic fields in three types of MRFs.

Figures 15 and 18 indicated that no obvious particle chains were formed in GH-MRF-250 and GH-MRF-350 when the magnetic field strength was 6 mT, but the tendency of particles to align with the magnetic field could be clearly observed on the surface and interior. The average particle chain lengths of GH-MRF-250 and GH-MRF-350 in a 6 mT magnetic field were only 0.5 mm and 0.8 mm. Figure 21 indicated the chain structures of GH-MRF-450 could be clearly observed, and the clusters-like structures began to form in a 6 mT magnetic field, the average particle chain lengths of GH-MRF-450 reached 2.8 mm. Figures 16 and 19 indicated that the obvious chain structures were formed in GH-MRF-250 and GH-MRF-350 when the magnetic field strength was 12 mT, and the average particle chain lengths of GH-MRF-250 and GH-MRF-350 in a 12 mT magnetic field were 1.1 mm and 1.4 mm. The number of the particle chains in GH-MRF-350 was greater than GH-MRF-250. Compared with Figure 21, Figure 22 indicated that the particle chain lengths increased rapidly in GH-MRF-450 when the magnetic field strength was 12 mT, which bridged the inner diameter of the container, and the dense clusters-like structure was formed. Figures 17 and 20 indicated that the particle chain structures increased apparent in an 18 mT magnetic field compared with Figures 16 and 19, the average particle chain lengths of GH-MRF-250 and GH-MRF-350 in an 18 mT magnetic field were 1.8 mm and 2.2 mm. Figure 23 indicated the denser clusters-like structures were formed in GH-MRF-450 when the magnetic field was 18 mT. In this state, the particle chains and the clusters-

like structures tightly connected, which nearly presented a cluster structures completely. The experiments indicated that the when an external magnetic field was applied, the magnetic particles began to form chains. Even in a magnetic field of only 6 mT, this phenomenon still clearly occurred, and the chain structures became more obvious with the increasing magnetic field. Meanwhile, the number of individual particles began to decrease, and the number of long chains began to increase, which was consistent with the simulation. The chain structures became increasingly apparent with the increasing particle volume fraction under the same external magnetic field, which was also consistent with the simulation. In Figure 24, the variation curve of GH-MRF-450 was exhibited with a different line type was that the particle chain lengths exceeded 10 mm in 12 mT and 18 mT magnetic fields, which bridged the inner diameter of the container. Figure 24 indicated that the particle chain lengths of MRF with high particle volume fractions increased sharply with the magnetic field.

5. Conclusions

In this study, the particles dynamics of MRFs in a magnetic field were analyzed, the model for the particle motion was proposed, and the particle distributions of the MRFs in different external magnetic fields were simulated. Furthermore, the same conditions were experimentally reproduced using industrial CT to study the microscopic characteristics of MRFs.

(1) The proposed motion model is able to intuitively simulate the microscopic characteristics of MRFs in magnetic fields in three-dimension, and the variations of particle chains of MRFs with different particle number under different magnetic fields could be extracted in the simulations.

(2) The application of industrial CT is an efficient method to clearly and intuitively study the microstructure of MRFs, meanwhile, the particle chains lengths of MRFs with different volume fractions in magnetic fields could be quantificationally captured by the industrial CT.

(3) The numerical simulations and industrial CT experiments indicate that the chain structure of the MRF particles becomes more apparent with increasing magnetic field strength, and in the same external magnetic field, the chain structure also becomes more apparent with an increase in the particle volume fraction.

(4) The particle chain lengths of MRF with high particle volume fractions increase sharply with the magnetic field.

6. Future work

In this paper, the microscopic properties of MRFs in magnetic fields were studied in detail. However, the microstructure of MRFs and its evolution in working state are extremely complex, which are also influenced by many factors, such as operating temperatures, shear and squeezing actions. In order to understand the properties of MRFs more comprehensively and deeply, the theoretical models about microstructure of MRFs under different influence factors should be further investigated, the numerical simulations considering these influence factors should be performed, and the relevant experimental devices in these aspects also need to be developed in the future.

Acknowledgements

The support of Fundamental Research Funds for the Central Universities (No. 2019BSCX12).

Conflict of interests

The authors declare that there is no conflict of interests regarding the publication of this article.

References

[1] Wang N N, Liu X H, Krolczyk G, et al. Effect of temperature on the transmission characteristics of high-torque magnetorheological brakes[J]. Smart Materials and Structures, 2019, 28(5): 057002.

[2] Ismail R, Ariyanto M, Perkasa I, Adirianto R, Putri FT, Glowacz A, Caesarendra W. Soft elbow exoskeleton for upper limb assistance incorporating dual motor-tendon actuator[J]. Electronics, 2019, 8(10): 1184.

[3] Esmaeilnezhad E, Hajiabadi S H, Choi H J. Effect of medium viscosity on rheological characteristics of magnetite-based magnetorheological fluids[J]. Journal of Industrial and Engineering Chemistry, 2019, 80: 197-204.

[4] Anupama A V, Kumaran V, Sahoo, B. Magnetorheological fluids containing rod-shaped lithium-zinc ferrite particles: the steady-state shear response[J]. Soft Matter, 2018, 14(26): 5407-5419.

[5] Gang H G, Choi S B, and Sohn J W. Experimental performance evaluation of a MR brake-based haptic system for teleoperation[J]. Frontiers in Materials, 2019, 6: 25.

[6] Rahman M, Ong Z C, Julai S, et al. A review of advances in magnetorheological dampers: their design optimization and applications[J]. Journal of Zhejiang University-Science A, 2017, 18(12): 991-1010.

[7] Zhang Y J, Li D C, Chen Y B, et al. A comparative study of ferrofluid seal and magnetorheological fluid seal[J].

IEEE Transactions on Magnetics, 2018, 54(12): 4601207.

[8] Zhong X L, Fan B, and Wu F. High-accuracy process based on the corrective calibration of removal function in the magnetorheological finishing[J]. Optical Engineering, 2017, 56(8): 084109.

[9] Sharma P, Chattopadhyaya, S, Singh N K. A review on magnetically supported gas metal arc welding process for magnesium alloys[J]. Materials Research Express, 2019, 6(8): 082002.

[10] Kumar R, Chattopadhyaya S, Agrawal B P, et al. Effects of types of GTAW including superior GTAW-PC with superimposed HF current on mechanical and metallurgical properties of super duplex stainless steel weld joints[J]. Materials Research Express, 2019, 6(7): 076572.

[11] Ji D S, Luo Y P, Ren H J, et al. Numerical simulation and experimental analysis of microstructure of magnetorheological fluid[J]. Journal of Nanomaterials, 2019, 2019: 6312606.

[12] Zhao P H, Fu Y Z , Li H L, et al. Three-dimensional simulation study on the aggregation behavior and shear properties of magnetorheological fluid[J]. Chemical Physics Letters, 2019, 722: 74-79.

[13] Samal S, Skodova M, Blanco I. Effects of filler distribution on magnetorheological silicon-based composites[J]. Materials, 2019, 12(18): 3017.

[14] Damiani R and Sun L Z. Microstructural characterization and effective viscoelastic behavior of magnetorheological elastomers with varying acetone contents[J]. International Journal of Damage Mechanics, 2017, 26(1): 103-117.

[15] Cvek M, Kracalik M, Sedlacik M, et al. Reprocessing of injection-molded magnetorheological elastomers based on TPE matrix[J]. Composites Part B: Engineering, 2019, 172: 253-261.

[16] Bodelot L, Voropaieff J P, Possinger T. Experimental investigation of the coupled magneto-mechanical response in magnetorheological elastomers[J]. Experimental Mechanics, 2018, 58(2): 207-221.

[17] Vagberg D and Tighe B P. On the apparent yield stress in non-Brownian magnetorheological fluids[J]. Soft Matter, 2017, 13(39): 7207-7221.

[18] Tian T F, Nakano M. Fabrication and characterisation of anisotropic magnetorheological elastomer with 45° iron particle alignment at various silicone oil concentrations[J]. Journal of Intelligent Material Systems and Structures, 2018, 29(2): 151-159.

[19] Hu T, Xuan S H, Ding L, et al. Stretchable and magneto-sensitive strain sensor based on silver nanowire-polyurethane sponge enhanced magnetorheological elastomer[J]. Materials and Design, 2018, 156: 528-537.

[20] Pei L, Pang H M, Ruan X H, et al. Magnetorheology of a magnetic fluid based on Fe_3O_4 immobilized SiO_2

core–shell nanospheres: experiments and molecular dynamics simulations[J]. RSC Advances, 2017, 7(14): 8142-8150.

[21] Zhao Y, Lv R Q, Li H, et al. Simulation and experimental measurement of magnetic fluid transmission characteristics subjected to the magnetic field[J]. IEEE Transactions on Magnetics, 2014, 50(5): 4600107.

[22] Gharibvand A J, Norouzi M, Shahmardan M M. Dissipative particle dynamics simulation of magnetorheological fluids in shear flow[J]. Journal of the Brazilian Society of Mechanical Sciences and Engineering, 2019, 41(2): 103.

[23] Lagger H G, Bierwisch C, Moseler M. MRF in a plate-plate magnetorheometer: Numerical insight into the particle-wall interface[J]. Journal of Physics: Conference Series, 2013, 412: 012020.

[24] Hajalilou A, Mazlan S A, Shilan S T, et al. Enhanced magnetorheology of soft magnetic carbonyl iron suspension with binary mixture of Ni-Zn ferrite and Fe3O4 nanoparticle additive[J]. Colloid and Polymer Science, 2017, 295(9): 1499-1510.

[25] Xu J H, Li J Y, Zhu P Z, et al. Coarse-grained molecular dynamics simulations of particle behaviors in magnetorheological polishing fluid[J]. Computational Materials Science, 2019, 163: 68-81.

[26] Liu X H, Liu Y Z, Liu H. Magnetorheological fluids particles simulation through integration of Monte Carlo method and GPU accelerated technology[J]. CMES-computer modeling in engineering and sciences, 2013, 91(1): 65-80.

[27] Li R, Li X, Li Y Y, et al. Experimental and numerical study on surface roughness of magnetorheological elastomer for controllable friction[J]. Friction, 2019.

[28] Xu Z Q, Wu H, Wang Q L, et al. Study on movement mechanism of magnetic particles in silicone rubber-based magnetorheological elastomers with viscosity change[J]. Journal of Magnetism and Magnetic Materials, 2020, 494: UNSP 165793.

[29] Chen S and Yang J. Probing Slip Differential Heat of Magnetorheological Fluids Subjected to Shear Mode Operation and Its Effect on the Structure[J]. Materials, 2019, 12(11): 1860.

[30] Tang B W, Gao S, Wang Y G, et al. Pore structure analysis of electrolytic manganese residue based permeable brick by using industrial CT[J]. Construction and Building Materials, 2019, 208: 697-709.

[31] Cui J, Liu D M, Cai Y D, et al. Insights into fractures and minerals in subbituminous and bituminous coals by FESEM-EDS and X-ray mu-CT[J]. Fuel, 2019, 237: 977-988.

[32] Kou B Q, Cao Y X, Li J D, et al. Granular materials flow like complex fluids[J]. Nature, 2017, 551(7680): 360-

+.

[33] Zhao C W, Peng X H, Huang J, et al. An enhanced dipole model based micro-macro description for constitutive behavior of MRFs[J]. Computers Materials and Continua, 2012, 30(3): 219-236.

[34] Melle S, Calderon O G, Rubio M A, et al. Rotational dynamics in dipolar colloidal suspensions: video microscopy experiments and simulations results[J]. Journal of Non-Newtonian Fluid Mechanics, 2002, 102 (2): 135-148.

[35] Zhou J F, Zhang H, Shao C L. Flow and heat transfer performances of dilute magnetorheological fluid flowing through hot micro channel[J]. International Journal of Heat and Mass Transfer, 2017, 107: 1035-1043.

[36] Lee S H. Ionic mobilities of Na+ and Cl- at 25 degrees C as a function of Ewald sum parameter: a comparative molecular dynamics simulation study[J]. Molecular Simulation, 2019.

[37] Tanygin B. Langevin dynamics simulation with dipole-dipole interactions: Massive performance improvements and advanced analytical integrator[J]. Computer Physics Communications, 2019, 235: 169-178.

[38] Martin J E, Anderson R A, Tigges C P. Simulation of the athermal coarsening of composites structured by a uniaxial field[J]. Journal of Chemical Physics, 1998, 108(18): 7887-7900.